

Quantitative phase imaging in biomedicine

YongKeun Park^{1,2,3}, Christian Depeursinge^{4,5} and Gabriel Popescu^{6*}

Quantitative phase imaging (QPI) has emerged as a valuable method for investigating cells and tissues. QPI operates on unlabelled specimens and, as such, is complementary to established fluorescence microscopy, exhibiting lower phototoxicity and no photobleaching. As the images represent quantitative maps of optical path length delays introduced by the specimen, QPI provides an objective measure of morphology and dynamics, free of variability due to contrast agents. Owing to the tremendous progress witnessed especially in the past 10–15 years, a number of technologies have become sufficiently reliable and translated to biomedical laboratories. Commercialization efforts are under way and, as a result, the QPI field is now transitioning from a technology-development-driven to an application-focused field. In this Review, we aim to provide a critical and objective overview of this dynamic research field by presenting the scientific context, main principles of operation and current biomedical applications.

Imaging biological cells and tissues is central to biological research and medical diagnosis. Following its four-century-old history, microscopy has become the most commonly used tool in medicine and biology¹. However, despite significant breakthroughs, optical imaging of biological specimens remains an active research field, aiming to exceed current spatial and temporal resolution, contrast, penetration depth, molecular specificity and quantitative capabilities. Quantitative phase imaging (QPI)² is emerging as a powerful, label-free approach to imaging cells and tissues, especially because it combines qualities found in microscopy, holography and light-scattering techniques: nanoscale sensitivity to morphology and dynamics, 2D, 3D and 4D (that is, time-resolved tomography) non-destructive imaging of completely transparent structures, and quantitative signals based on intrinsic contrast. Here, we review the context in which the QPI field developed, the main principles of operation, and representative basic and clinical science applications. We end with a summary and outlook of the field.

In 1873, the first theory of image formation in an optical microscope was established by Abbe³. The idea that imaging is formed by the superposition of waves emerging at different angles from a sample was new and powerful: it established that the image is a (complicated) interferogram. The result also implied that a microscope could not resolve objects smaller than half the wavelength, when using propagating waves. This resolution dogma remained essentially unchallenged for more than a century, until Hell and Wichmann's paper in 1994 (ref. ⁴). Therefore, the other crucial metric of imaging, contrast, can be credited with the tremendous developments in microscopy over its long history¹. Contrast defines how clearly a subject of interest is distinguished from the background. For a biological specimen, the thickness and refractive index inhomogeneity determine how much light scattering it produces. It is scattering rather than absorption that determines the ultimate contrast of the image, as in the visible spectrum most cells and tissues do not absorb significantly⁵. Too little scattering from the specimen makes it challenging to reveal the structure from an overwhelming incident light background, while too strong a scattered component

will wash out the image altogether due to multiple scattering. Both of these extremes result in poor image contrast. Single cells and thin tissue slices belong to the first category: the scattered light they generate is orders of magnitude weaker than the incident light. This class of specimens is referred to as 'phase objects', as they affect significantly only the phase of the incident field and not the amplitude. To render such structures visible, one solution was to convert them into 'amplitude objects' using various stains or fluorescent tags^{6,7}. Today, the gold standard of histopathology is performing manual diagnosis on stained, several-micrometre-thick tissue slices, while fluorescence microscopy is the main imaging tool in cell biology⁶. However, while stains and tags offer high-contrast imaging with molecular specificity, they are often qualitative and sample-preparation-dependent, while photobleaching and phototoxicity limit fluorescent imaging of live cells. Furthermore, the use of exogenous labelling agents, such as fluorescent proteins or dyes, may alter the normal physiology of cells and, furthermore, labelled cells cannot be re-injected into the human body. These limitations may hinder advances in neuroscience, stem cell research and immunotherapy, to name just a few.

A major advance in intrinsic contrast imaging occurred in the 1930s, when Zernike invented a technique capable of imaging phase objects with high contrast and without the need for tagging⁸. The principle of Zernike's phase contrast microscopy builds on Abbe's understanding of imaging as an interference process. Specifically, the incident and scattered fields are treated as, respectively, the reference and object wave of an interferometer (see, for example, ref. ⁹, page 472). Thus, the total field, U , has the form:

$$U(x, y) = |U| e^{i\phi(x, y)} \approx |U| [1 + i\phi(x, y)] \quad (1)$$

where $\phi(x, y)$ is the phase delay map of a sample. Note that the intensity image of such an object, $|U|^2$, exhibits little spatial modulation, that is, no contrast. To boost the contrast of the resulting interferogram, and thus the image, Zernike added a further $\pi/2$ phase shift between the two. The additional $\pi/2$ shift places the scattered field

¹Department of Physics, Korea Advanced Institute of Science and Technology (KAIST), Daejeon, Republic of Korea. ²KAIST Institute for Health Science and Technology, Daejeon, Republic of Korea. ³Tomocube Inc., Daejeon, Republic of Korea. ⁴Microvision and Microdiagnostic Group (SCI STI CHD), Ecole Polytechnique Fédérale de Lausanne (EPFL), Lausanne, Switzerland. ⁵Laboratory for Cellular Imaging and Energetics, Biological and Environmental Sciences and Engineering Division, King Abdullah University of Science and Technology (KAUST), Thuwal, Saudi Arabia. ⁶Departments of Electrical and Computer Engineering and Bioengineering, Beckman Institute for Advanced Science and Technology, University of Illinois at Urbana-Champaign, Urbana, IL, USA.

*e-mail: gpopescu@illinois.edu

in antiphase with respect to the incident field, such that the phase contrast image field becomes:

$$U_{PC}(x, y) = |U| \{1 + i[i\phi(x, y)]\} \approx |U| e^{-\phi(x, y)} \quad (2)$$

Due to the additional $\pi/2$ phase shift, the resulting phase contrast field converts the phase into amplitude modulation (the complex exponential was converted into a real exponential). Currently, phase contrast microscopes also balance the power of the two fields by attenuating the incident field. These simple modifications provided the microscope with the ability to visualize in high detail live, unlabelled cells and other transparent objects. Today, the phase contrast microscope is broadly used in most cell biology laboratories.

In 1948, when Gabor proposed using an optical approach to correct spherical aberrations in electron micrographs, perhaps he did not anticipate that holography would become an area of research in itself, most productively used in the optical region of the spectrum¹⁰. Gabor showed that recording the intensity of the light emerging from an object at an out-of-focus plane incorporates both amplitude and phase information about the field at the image plane. When a recording film is illuminated by the same incident wave, the image of the object is recreated at a certain distance away from the film. The appearance of the 3D light distribution in space via parallax generated a broadly spread confusion that holography is synonymous with 3D imaging. As we show in this Review, holography data can be used to obtain the 3D structure of a transparent object, but a single hologram is not sufficient for this purpose.

It soon became apparent that Gabor's in-line holography suffered from a severe limitation: in addition to the in-focus image, the method always generated an overlapping out-of-focus 'twin' image, which was detrimental. The images appear in pairs essentially because the intensity signal is generated by pairs of counter-propagating waves, in other words, the Fourier transform of a real signal is a Hermitian function. The problem of the 'twin' image was solved by Lohmann¹¹ and Leith and Upatnieks¹². They proposed using an off-axis incident field, which, in the end, shifts the unwanted image onto a different axis with respect to the in-focus image. As described below, today the recording media and image reconstructions are now digital, and the field is known as digital holography¹³. Its application to microscopy is known as digital holographic microscopy (DHM)¹⁴, which provided early QPI images of inorganic samples¹⁵.

Precursors to QPI

It became apparent that by combining holography and microscopy, one can perform highly sensitive measurements of the thickness and refractive index of biological specimens, much like in metrology¹⁶. Early on, such quantitative phase measurements were performed by single-point, scanning techniques, building on the advancement of optical coherence tomography (OCT)¹⁷. Polarization-sensitive OCT¹⁸ and Doppler OCT¹⁹ can be regarded as two important precursors to OCT-based QPI. Polarization-sensitive OCT detects relative phase shifts between two polarizations of light (birefringence) and Doppler OCT measures the time derivative of phase change due to moving objects, that is, a frequency shift (or Doppler shift). Using two polarization channels to encode relative phase information, differential phase contrast in OCT²⁰ was demonstrated. Yang et al. developed a phase-dispersion microscope, whereby the phase difference between the fundamental and second-harmonic light, both interacting with the specimen, was quantified, thus, reducing phase noise²¹. Later, this method was advanced to yield quantitative phase measurements²².

Later on, two independent papers reported on using spectral domain OCT to achieve QPI for studying cell structure and dynamics^{23,24}. Point-scanning techniques benefit from the ease of implementation and can leverage existing OCT instruments, but suffer from low throughput and noise introduced by the

mechanical instability of the scanning process. To eliminate scanning, researchers devoted efforts towards developing full-field QPI methods, in which the phase map across a field of view is retrieved simultaneously.

Full-field QPI and figures of merit

The full-field methods can be grouped into two classes, according to the phase shifting (Fig. 1a) and off-axis (Fig. 1b) holography geometry from which they originate. Unlike in holography, where the goal is to record a mixed phase and amplitude signal that is then used to reconstruct the image of the object, QPI extracts the phase map associated with the object, decoupled from the intensity information. In the first type of approach, QPI images can be obtained directly in the focal plane by in-line geometries used in combination with temporal phase shifting, in which the time delay of the reference is controllably incremented, and several corresponding intensity images are recorded (Fig. 1a). The irradiance at the detector is:

$$I(x, y) = I_0 + I_1(x, y) + 2\sqrt{I_0 I_1(x, y)} \cos[\omega\tau + \phi(x, y)] \quad (3)$$

where I_0 and I_1 are the irradiances for the reference phase wave and object field, respectively, ω is the angular frequency of the optical field and τ is the time delay between the two waves. In general, the phase image ϕ can be determined from four intensity measurements corresponding to $\omega\tau = 0, \pi/2, \pi, 3\pi/2$ (Fig. 1c,d) as:

$$\phi = \arg(I_0 - I_\pi, I_{3\pi/2} - I_\pi) \quad (4)$$

Other numbers of frames have been used in phase-shifting interferometry (see, for example, ref. ¹⁶ for a review). Clearly, phase-shifting methods are limited in throughput due to the serial detection of several frames.

A spatial case of phase-shifting interferometry is based on the transport of intensity equation, which connects the axial gradient of the intensity with the transverse Laplacian of the phase. Normally, two intensity images (one in focus, one slightly out of focus) are sufficient to obtain the Laplacian of the phase image, which must be further integrated numerically, under certain assumptions²⁵. This method is very easy to implement, but suffers from poor recovery of low frequencies (only the second-order derivative is measured). Furthermore, the transport of intensity equation is based on the small angle approximation, which is strictly valid only for low-resolution imaging (see section 12.1 in ref. ² for the derivation). Sometimes this method is referred to as 'non-interferometric'. However, the phase information is still revealed by the interference between the incident and scattered light, which is also the starting point for phase contrast microscopy.

Off-axis interferometry exploits spatial rather than temporal modulation and, as a result, yields a phase map from a single intensity recording (Fig. 1b). The irradiance of the interferogram is:

$$I(x, y) = I_0 + I_1(x, y) + 2\sqrt{I_0 I_1(x, y)} \cos[\alpha x + \phi(x, y)] \quad (5)$$

where I_0 and I_1 are the intensities of the reference (assumed a plane wave) and image field, respectively, α is the spatial frequency introduced by the off-axis angle θ , $\alpha = 2\pi \sin(\theta)/\lambda$, and λ is the wavelength of light. Because of the modulation frequency α , the cross-term containing the phase can be isolated via a Fourier transform, followed by a single sideband frequency filter, and an inverse Fourier transform²⁶, as outlined in Fig. 1e-g. Off-axis methods have also been combined with (spatial) phase shifting²⁷.

The clear advantage of off-axis methods is the single-shot capability, which allows for high-speed imaging. However, this boost in

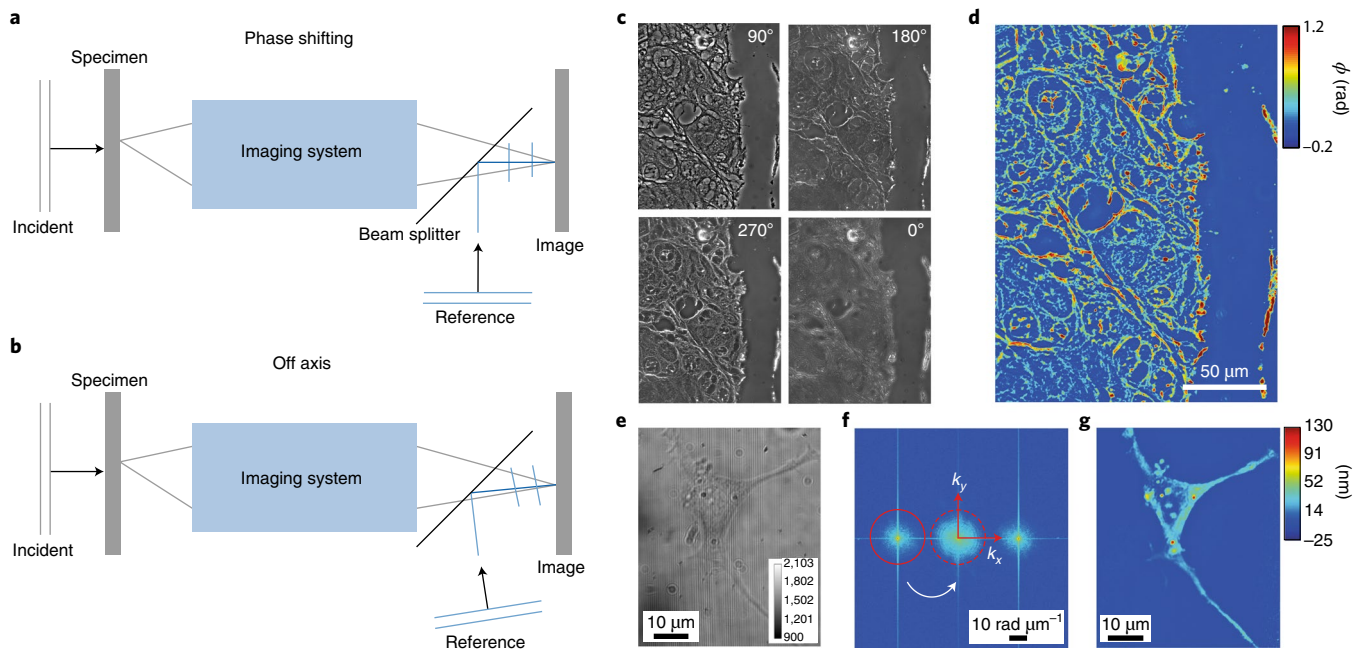


Fig. 1 | Principles of QPI measurements. **a**, Phase shifting QPI: the reference field is in-line with the imaging field. **b**, Off-axis QPI: the reference field is tilted to create spatial modulation. **c**, Individual frames recorded in phase-shifting interferometry. **d**, QPI image resulting from combining the four frames in **c**. Colour bar indicates phase shift in radians. **e**, Interferogram from an off-axis system. Values are arbitrary units. **f**, The Fourier transform of the image in **e**. One of the high orders is preserved (the rest is filtered out) and shifted to the baseband. **g**, Resulting phase image of a neuron, obtained by inverse Fourier transforming the signal in **f**. Colour bar indicates optical path length in nanometres. k_x and k_y correspond to the spatial frequency along the x and y axes, respectively. Panels **a** and **b** adapted from ref. ², McGraw-Hill Education.

the time–bandwidth product comes at the expense of the space–bandwidth product. As a result, both approaches are currently used broadly; the optimal choice depends on the application of interest. In addition to the time–bandwidth and space–bandwidth product characteristics, phase sensitivity, both temporally and spatially, plays a crucial role in the operation of QPI methods. Below we describe these properties in more detail.

Temporal phase sensitivity, governed by the phase stability of the instrument, is the most challenging feature to achieve in QPI. This characteristic defines the smallest temporal phase shift that an instrument can detect (see section 8.5.3 in ref. ²). This is an age-old challenge, as Michelson and Morley stated it as early as 1887: “In the first experiment one of the principal difficulties encountered was [...] its extreme sensitivity to vibration. This was so great that it was impossible to see the interference fringes except at brief intervals when working in the city, even at two o’clock in the morning.”²⁸

Temporal phase noise is due to the path length difference between the reference and object beams, which fluctuates randomly in time due to mechanical vibrations, surrounding air fluctuations and so on, but also due to electronic noise that occurs in the detection and digitization process. The ultimate limit is set by shot noise, which is a manifestation of photon statistics at the detector²⁹. Exceeding this limit can be achieved by averaging in space and time. Significantly, successful noise suppression efforts by the Laser Interferometer Gravitational-Wave Observatory group resulted in an optical path length sensitivity of less than 10^{-9} nm, which allowed for the first experimental observation of gravitational waves³⁰. In QPI, passive (using damped optical tables, mechanically secured optical components and so on) as well as active (negative feedback loops) methods of stabilization have been used. More recently, common-path approaches have exploited the central idea in phase contrast microscopy: the incident light acts as a reference field locked in-phase with the scattered field, which results in intrinsic stability^{31–33}. Also, a method of common-path single-pixel quantitative phase

and absorption microscopy was demonstrated³⁴. These methods benefit from cancelling the noise before it is detected, thus, providing robust instruments for long-term biological studies. However, common-path methods bring on a different type of challenge: as the incident light is the reference of the interferometer, accurate phase information requires high spatial coherence over the entire field of view. While this condition can be achieved using lasers, spatially filtering an extended source to a plane wave dramatically reduces the incident power. Typically, as is the case with phase contrast microscopy, spatial coherence is traded for manageable power levels. As a result, the incident, or reference field, contains low-frequency components that are then subtracted from the final image, which essentially becomes a high-pass version of the original. This effect is known as the halo artefact, and several methods have been proposed to correct it³⁵.

Spatial phase sensitivity in QPI defines the smallest phase step that is detectable in a given frame, and is limited by the amount of background noise present in the field of view. While the sample preparation itself can add to the spatial noise level (for example, debris in cell culture media), the fundamental source of intrinsic optical noise is due to speckle. This phenomenon represents spatial intensity fluctuations due to the superposition of spurious fields that interfere at the detector. Clearly, with increased spatial and temporal coherence of the incident fields, there are a larger number of waves that contribute to the interferogram, and a higher-contrast speckle pattern emerges, washing out the high-frequency components of the image. Speckles can be averaged out, either spatially by illuminating with a diversity of \mathbf{k} -vectors via diffusers³⁶, or temporally, by using broad optical spectrum illumination, or both³². It has been shown that the highest spatial sensitivity in QPI is obtained using white-light illumination, exploiting the uniform background exhibited by phase contrast microscopy. In sum, using highly coherent sources reduces halo artefacts but they are plagued by speckles, resulting in low-passed quantitative phase images, while

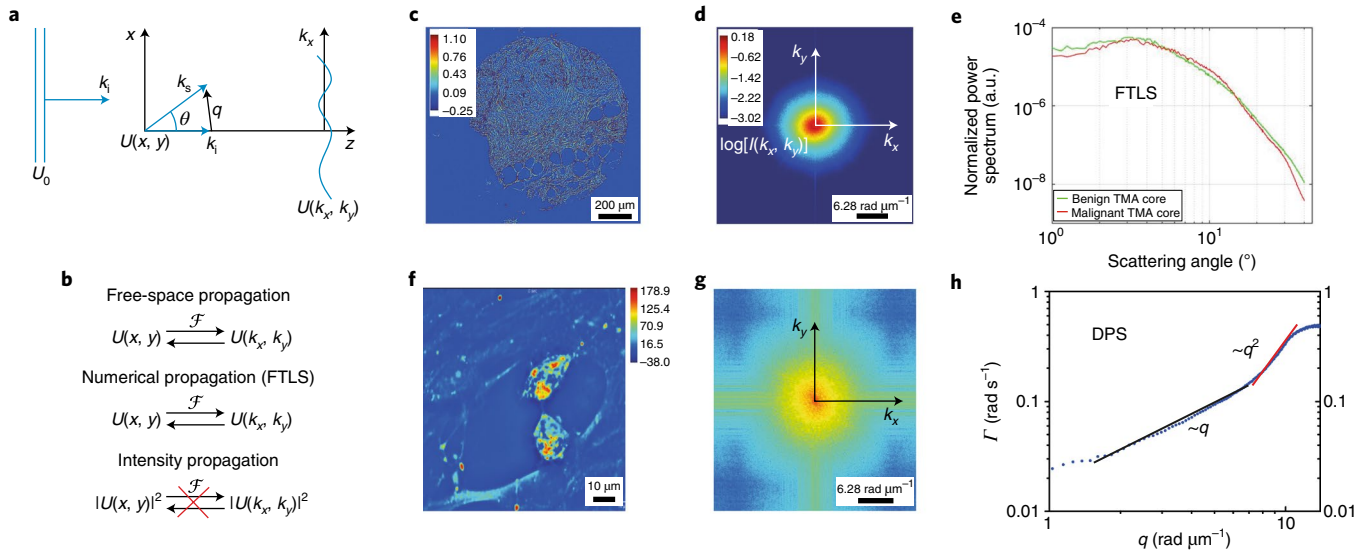


Fig. 2 | Converting QPI into light-scattering information. **a**, Light scattering geometry. U_0 is the incident field, k_i is the incident wavevector and k_s is the scattering wavevector. **b**, Illustration of the fact that retrieving scattering information from the measured image and vice versa can only happen if the complex field is known. **c**, A phase image associated with a tissue core (colour bar indicates phase shift in radians). **d**, The power spectrum $I(k_x, k_y)$ of the complex field shown in **c** (colour bar indicates log of the power spectrum, in arbitrary units). **e**, Spatial power spectrum plotted against the scattering angle θ , up to the objective numerical aperture (approximately 45°). **f**, A frame from a time-lapse quantitative phase image of two microglia cells in culture (colour bar indicates optical path length in nm). **g**, Fourier transform of the field in **f**. **h**, DPS curve associated with the timelapse image in **f**. The q and q^2 behaviour indicate deterministic and diffusive transport, respectively.

using incoherent illumination results in high-resolution but high-passed images.

It is evident that the performance of a QPI system is defined by the compromise of these four figures of merit: space–bandwidth product, time–bandwidth product, spatial phase sensitivity and temporal phase sensitivity. While each of these parameters is maximized, respectively, by phase-shifting interferometry, off-axis interferometry, broadband illumination and common path geometry, there are QPI approaches that are optimized for more than one^{37–39} (see also section 8.6. in ref.²). Sensitivity evaluation in QPI, including theoretical sensitivity limit (Cramér–Rao bound) is discussed in ref.⁴⁰.

Recently, it has been demonstrated that a neural network is capable of obtaining the phase from intensity signals generated by unknown objects^{41,42}. It is speculated that the neural network learns both the priors about the class of objects represented in its training examples and the physical model of propagation. It will be interesting to observe in the future how machine-learning methods will deal with physical problems that inherently present non-unique solutions, such as extracting phase from amplitude signals (see, for example, ref.⁴³ for recently addressing this issue).

QPI-enabled scattering measurements

One of the exciting features of QPI is that it can turn an imaging instrument into a powerful scattering measurement device. This feature only happens because the optical field data allows us to numerically convert an image (spatial domain) into angular scattering (spatial frequency domain) information. As a result, QPI becomes an even richer field, covering not just imaging applications, but also static and dynamic light-scattering studies, traditionally covered by separate instruments.

Angular light scattering using QPI. In general, angular light-scattering measurements provide information about the Fourier transform of the field at the object plane (Fig. 2). As a result, angle-resolved intensity measurements of the scattered light

depend on the phase of the object field, which in turn yields information about the internal structure of objects, even when they are completely transparent. Due to the ability to study inhomogeneous and dynamic samples through direct intensity measurements, light-scattering methods have been used broadly, from atmospheric science to soft condensed-matter physics and biomaterials⁴⁴. Note that the Fourier relationships between the image and scattered light only apply to complex fields, not intensities (Fig. 2a,b). Measuring the intensity distribution at the scattering plane does not provide the intensity distribution at the image plane, and vice versa. However, using QPI, one can retrieve both the phase and amplitude of the image field, which can further be Fourier transformed numerically to obtain the scattered field. This approach, referred to as Fourier transform light scattering (FTLS)⁴⁵ is the spatial analogue of Fourier transform (infrared) spectroscopy. The conversion from QPI data to scattering information can be easily understood by considering the inhomogeneous Helmholtz equation:

$$\nabla^2 U(\mathbf{r}, \omega) + n_0^2 \beta_0^2 U(\mathbf{r}, \omega) = -\beta_0^2 \chi(\mathbf{r}) U(\mathbf{r}, \omega) \quad (6)$$

where U is the sum of the incident and scattered fields, $U = U_0 + U_1$, \mathbf{r} the spatial coordinate, ω the angular frequency, n_0 the background refractive index, $\beta_0 = \omega/c$, with c the speed of light in vacuum, and $\chi(\mathbf{r}) = n^2(\mathbf{r}) - n_0^2$, the scattering potential, assumed to be non-dispersive. For a plane wave incident along z , $U_0(\mathbf{r}) = A(\omega) e^{i\beta_0 z}$, and weakly scattering objects, applying the first-order Born approximation, we obtain a simple solution for the forward scattered field:

$$U_1(\mathbf{k}_\perp, z; \omega) = -i\beta_0^2 A(\omega) e^{i\gamma z} \chi(\mathbf{r}_\perp, \gamma - \beta) / 2\gamma \quad (7)$$

where A is the spectral amplitude of the incident field, $\gamma = \sqrt{n_0^2 \beta_0^2 - k_\perp^2}$ and $\mathbf{k}_\perp = (k_x, k_y)$. For small angles of scattering, or

under the Fraunhofer region, that is, $k_{\perp} \ll \beta$, or $\gamma \neq \beta$, equation (7) simplifies to:

$$U_1(\mathbf{k}_{\perp}, z; \omega) \approx -i\beta_0/2A(\omega)e^{i\beta z}\chi(\mathbf{k}_{\perp}, k_z)|_{k_z=\omega} \quad (8)$$

$$= -i\beta_0/2A(\omega)e^{i\beta z} \int_{-L/2}^{L/2} \chi(\mathbf{k}_{\perp}, z) dz$$

Equation (8) indicates that the scattered field provides information about an axially projected object, with each transverse scattering wavevector, \mathbf{k}_{\perp} , corresponding to one spatial frequency from the object. Since in QPI one measures the complex field $U = U_0 + U_1$, it follows that $U_1(\mathbf{k}_{\perp})$ can be obtained by a simple Fourier transform of the complex image field. Figure 2c–e illustrates how phase images yield scattering data. Because in FTLS the measurement is performed at the image plane, where the field at each point is the superposition of all the \mathbf{k} -vector contributions, the measurement can be performed with high signal-to-noise ratio. Thus, light-scattering measurements performed this way are extremely sensitive and yield high dynamic range. For example, it is challenging to measure high-dynamic-range angular light scattering from a single cell using traditional, goniometer-based measurements, because the weak scattering from the cell is split further for each angular bin. However, it is very easy to image the cell with QPI and convert the data into FTLS (see chapter 13 in ref. ² for further details).

Dynamic light scattering using QPI determined from four intensity measurements. Dynamic light scattering is a powerful method for characterizing weakly scattering, dynamic systems⁴⁶. Traditional approaches rely on measuring fluctuations in the scattered intensity at a fixed angle. The spectral bandwidth of these fluctuations, f , relates to the diffusive (random, passive) and advective (deterministic, active) motion of the scatterers:

$$\Gamma(q) = Dq^2 + \Delta\mathbf{v} \cdot \mathbf{q} \quad (9)$$

where D is the diffusion coefficient, $\Delta\mathbf{v}$ is the width of the velocity distribution along a certain direction and \mathbf{q} is the scattering wavevector (or momentum transfer), $\mathbf{q} = \mathbf{k} - \mathbf{k}_i$ (Fig. 2a), $q = 2\beta_0 \sin \theta/2$, where θ is the scattering angle. Note that, from measurements at a certain θ , the active and diffusive contributions may overlap. While measurements at multiple angles are possible using traditional goniometer-based instruments, obtaining the spatial frequency (q -domain) dependence is difficult in these approaches.

Using time-resolved QPI data, measuring the dispersion relation, $\Gamma(q)$, is practical. This approach, known as dispersion-relation phase spectroscopy (DPS), allows dynamic studies in living systems⁴⁷. Figure 2f–h illustrates this method with results on live cells in culture. It can be seen that, at high q values (short distances), the intracellular transport is diffusive, while at low q values, the transport becomes deterministic (Fig. 2h). These results indicate that over long distances (low q), the mass transport requires active, molecular-motor-driven transport, for which diffusion is too slow. Note that, unlike particle tracking methods, DPS can be applied to continuous (as well as discrete) media. As the data come from an imaging method, DPS can study regions of interest within the field of view, which might be characterized by different dynamics.

Tomographic QPI

Information about the complex scattered field can be used to extract tomographic information about the weakly scattering object. The determination of the 3D refractive index tomogram of a

semi-transparent object was given in a seminal theoretical paper of E. Wolf⁴⁸ in 1969, which was then experimentally demonstrated by A. Fercher et al.⁴⁹ in 1979. However, its applications to biology and medicine have grown largely since the 2000s.

The principle of tomographic QPI techniques is summarized below. Let us assume a plane wave incident along a direction, \mathbf{k}_i (Fig. 2a). Following the same procedure as for deriving equation (8), we obtain the scattering potential expression (see, for example, chapter 13 in ref. ⁹):

$$\chi(\mathbf{k}_{\perp} - \beta\mathbf{k}_{\perp i}, k_z)|_{k_z = \gamma - \beta\hat{k}_i \cdot \hat{z}} = -\frac{2\gamma}{\beta_0^2(\omega)A(\omega)} e^{-i\gamma z} U(\mathbf{k}_{\perp}, z; \omega) \quad (10)$$

Note that for plane wave illumination along z , $\hat{k}_{1,i} = 0, \hat{k}_{z,i} = 1$, we recover equation (7). From equation (10), we see that the axial information about the object is carried by the spatial frequency:

$$k_z = \gamma - \beta\hat{k}_i \cdot \hat{z} = \sqrt{\omega^2/c^2 - k_{\perp}^2} - n\omega/c \cos(\theta) \quad (11)$$

The performance of the tomographic reconstruction is governed by the sampling in k_z , as follows: the range (k_z^{\min}, k_z^{\max}) determines the z resolution, and the sampling step in k_z controls the overall depth of field. It is clear from equation (11) that varying either ω or θ , k_z can be varied and tomographic reconstruction can be achieved. That is to say, performing measurements either with broadband light or a variety of illumination angles (or both) can provide depth sectioning. For a fixed ω and θ , the microscope objective captures a range of angles from the sample, that is, a superposition of k_{\perp} , which results in a single projection through the object. The range in k_{\perp} , dictated by the objective numerical aperture, results in an image with the z information integrated over the respective depth of field. A series of techniques have been developed to measure the 3D distributions of refractive index of biological cells (Fig. 3a–d).

To scan the incident angle with respect to the sample ($\hat{\mathbf{k}}_{1,i}$ in equation (10)), several approaches have been reported for rotating the illumination beam with respect to the sample^{50–52} or rotating the sample with respect to the illumination^{53–55}. To achieve this, various devices have been utilized including a galvanometric mirror, a liquid-crystal-based spatial light modulator and, recently, a digital micromirror device. Different tactics have been introduced for the sample rotation, including mechanical rotation⁵⁴, holographic optical tweezers⁵⁶ and a microfluidic channel⁵⁷. In addition, an array of light-emitting devices has also been utilized in ptychography⁵⁸. The control of the temporal frequency of the illumination (ω in equation (11)) can also be utilized, which has been achieved by scanning the wavelength of the illumination⁵⁹ or controlling the coherence gating and optical coherence tomography^{60,61}. Recently, the theory of optical diffraction tomography has been extended to temporally incoherent light, which also provides access to optical sectioning³². Examples of live cell tomograms are illustrated in Fig. 3e–h.

To reconstruct a 3D refractive index tomogram from the measured multiple 2D QPI images described above, a reconstruction algorithm is employed. One common algorithm reconstructs the tomogram of almost transparent samples via the filtered back-projection method⁵¹. However, most biological samples, including individual cells, exhibit certain amounts of light diffraction, and thus the use of diffraction algorithm provides results with enhanced image quality⁴⁸. The diffraction algorithm inversely solved light diffraction, based on the first Born (equation (11)) or Rytov approximation, assuming weak scattering. A rigorous proof of a regularized inverse algorithm for coherence retrieval was presented in ref. ⁶². Recently, a neural-network-based algorithm has been introduced to solve the tomographic reconstruction⁶³.

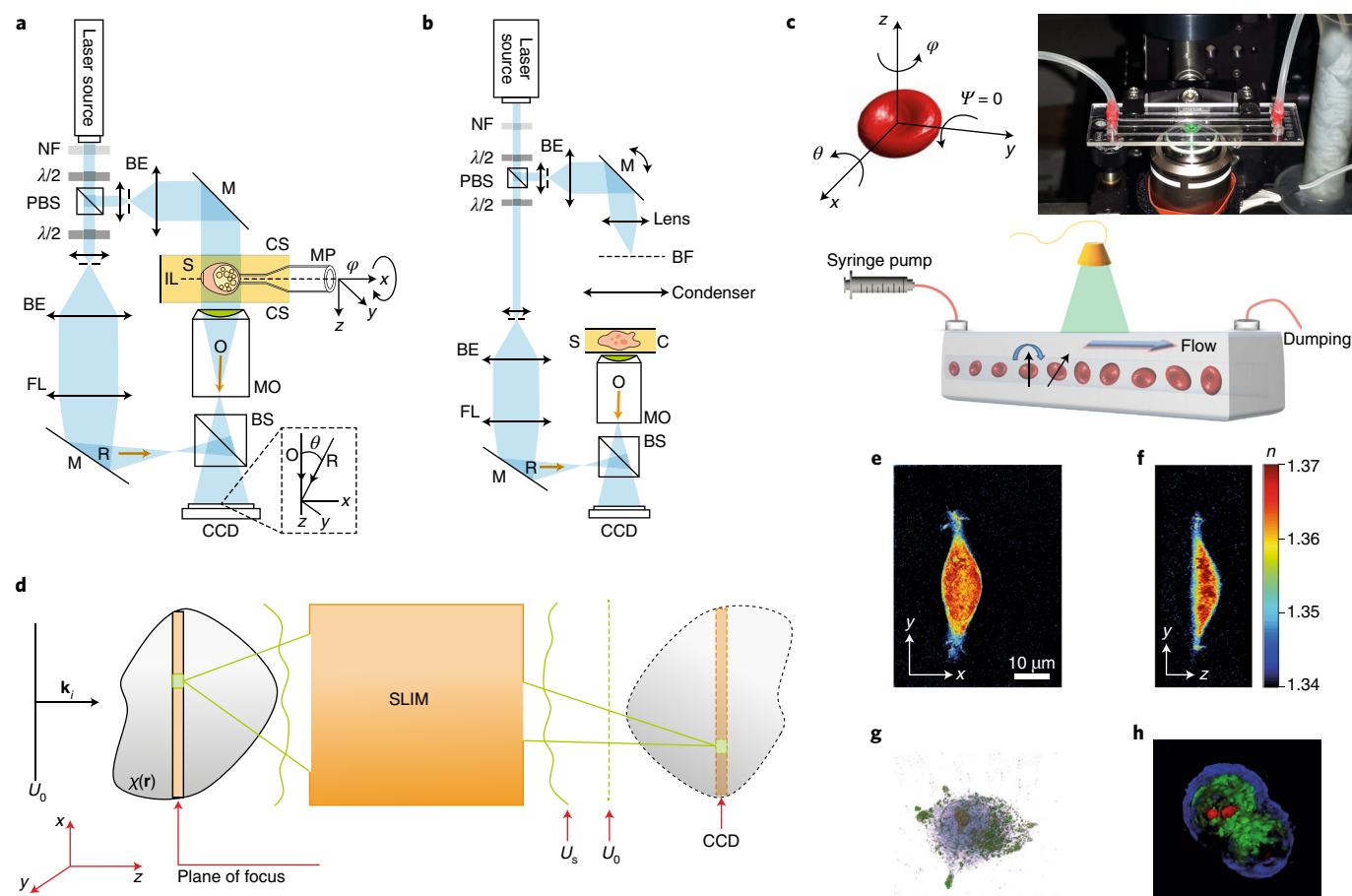


Fig. 3 | Approaches for tomographic QPI. a, The illumination is fixed, while the sample is rotated. **b**, The illumination angle is varied via a rotating mirror. NF, neutral filter; $\lambda/2$, half-wave plate; PBS, polarizing beam splitter; BE, beam expander; M, mirror; FL, focusing lens; S, sample; MP, micropipette; CS and C, coverslip; BF, back focal plane; MO, microscope objective; CCD, charge-coupled device camera; R, reference beam; O, object beam. **c**, A cell tumbles in a microfluidic channel, while the illumination is fixed. Top left: a single RBC in the coordinate system, with the three possible rotation angles. Ψ is the angle of rotation around y , θ and φ are around x and z , respectively. Top right: the experimental set-up with the microchannel in the vicinity of the objective. Bottom: illustration of the RBC tumbling in the microchannel. **d**, The plane of focus is scanned through a 3D specimen, while phase images are measured at each z position. U_s is the scattered field. **e–h**, Examples of tomograms reconstructed from live cells. **e**, Live cell imaged by QPI in the x - y plane. **f**, Same cell as in **e**, expect imaged in the y - z plane (colour bar indicates refractive index, n). **g**, 3D rendering of a live cell using QPI. **h**, 3D tomography of an HT29 cell using the approach described in **d**. Panels adapted from: **a, b**, ref. ¹⁴, Taylor and Francis Group LLC; **c**, ref. ⁵⁷, Springer Nature Limited. Panels reproduced from: **d, h**, ref. ³², Springer Nature Limited; **e, f**, ref. ¹²⁴, under a Creative Commons licence (<https://creativecommons.org/licenses/by/4.0/>); **g**, ref. ¹²⁵, under a Creative Commons licence (<https://creativecommons.org/licenses/by/4.0/>).

Super-resolution is an important goal in microscopy applied to life sciences. Complex field deconvolution was employed to enhance the spatial resolution⁶⁴. By imaging a nanohole and taking the complex wavefield yielded by an objective lens, the complex transfer function of an imaging system could be established precisely. Exploiting oblique illumination, this approach can extend the reach of the \mathbf{k} -spectrum in the wavevector space, improving the lateral resolution of QPI by a factor approaching two⁵².

Applications

Due to the tremendous progress in instrumentation development, QPI technologies are sufficiently robust to be employed in in-depth biomedical studies. In this section, we review representative basic and clinical science applications of QPI.

Basic science. One of the first demonstrations of QPI is based on the utility of optical phase for sensing cell structure and dynamics at the nanoscale. Due to this sensitivity of QPI for probing cell membrane dynamics, it has been applied to the study of red blood

cells (RBCs), as shown in Fig. 4a and detailed in chapter 11 of ref. ². As RBCs have distinct biconcave morphology without sub-cellular organelles, 2D QPI techniques are well suited to investigate their biophysical and pathophysiological properties.

This sensitivity to nanoscale changes in thickness was employed to study live neurons during electrical activity (Fig. 4b). Neuronal network activity was monitored optically by the phase signal^{65–67}. More precisely, neuronal activity could be investigated by the application of glutamate, which is the main excitatory neurotransmitter in the brain, released at 80% of the synapses. Practically, a QPI system equipped with electrophysiology set-up has been developed to study the early stage of neuronal responses induced by glutamate on primary culture of mouse cortical neurons. This study involving pharmacological experiments revealed that glutamate produces three distinct optical responses, predominantly mediated by NMDA (*N*-methyl-D-aspartate) receptors: biphasic, reversible decrease and irreversible decrease responses. Consistently, the phase decrease results from water entrance accompanying the influxes of Ca^{2+} and Na^+ for osmotic reasons. In another context,

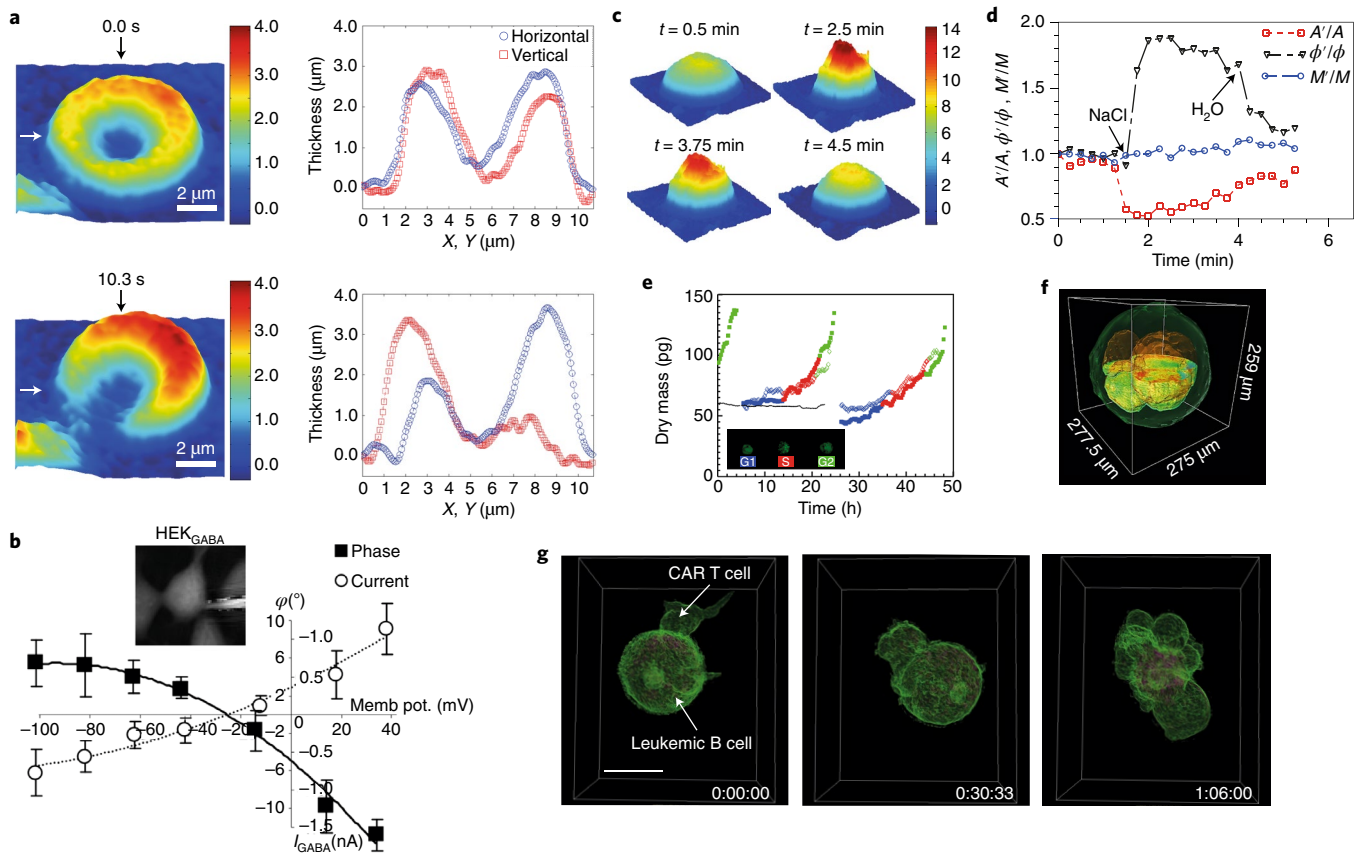


Fig. 4 | Applications of QPI in basic science. **a**, Dynamic profilometry of a RBC using QPI. The white arrows indicate the directions along which the profiles are plotted and the colour bars indicate phase shift in radians. **b**, The phase (φ) versus voltage (V) curve (squares and solid line) and the current (I) versus voltage (V) curve (circles and dotted line) obtained with GABA ($n = 7$) indicated an equilibrium potential for Cl^- of -26 mV (ref. ⁶⁶). Error bars obtained by repeated measurements of phase and current at various voltages V . Inset: representative quantitative phase image of a patched HEK cell obtained by digital holographic microscopy (DHM) ¹⁴. **c**, QPI of a live cell during osmotic changes. Colour bar indicates phase in radians. **d**, Relative change in area (red; A'/A), phase (black; φ'/φ) and dry mass (blue; M'/M) on applying NaCl and rinsing with water, as indicated. A' , φ' and M' represent the projected area, average phase shift and dry mass, respectively, while A , φ and M represent the initial values (at $t = 0$). **e**, Growth of a U2OS cell during various phases of the cell cycle: G1, blue; S, red; G2, green. **f**, Tomography of a bovine embryo, using GLIM. **g**, Time-lapse tomogram showing a chimeric antigen receptor (CAR) T-cell killing a cancer cell during a one-hour period. Scale bar, $5 \mu\text{m}$. Panel **b** adapted from ref. ⁶⁶, under a Creative Commons licence (<https://creativecommons.org/licenses/by/3.0/>). Panels reproduced from: **a**, ref. ¹¹⁰, SPIE; **c,d**, ref. ⁷¹, American Physiological Society; **e**, ref. ⁷⁸, NAS; **f**, ref. ³³, under a Creative Commons licence (<https://creativecommons.org/licenses/by/4.0/>).

experiments with human embryonic kidney (HEK) cells have validated the model of phase variations associated with Cl^- currents mediated by GABA (γ -aminobutyric acid) applications and have allowed the phase response to be constructed as a function of the clamped membrane potential, allowing the determination of the equilibrium potential for Cl^- with the same precision as an electrophysiological approach⁶⁶. Figure 4b illustrates the relationship between phase and transmembrane ionic currents in patched transfected HEK cells⁶⁶. The reversal potential for Cl^- could be derived from the phase shift evoked by GABA or muscimol application. The potential corresponding to the ionic current reversal was found around 26 mV, close to the accepted value of 33 mV derived from the Nernst equation.

Perhaps one of the most impactful applications of QPI to date is measuring single-cell volume and mass, non-destructively, over arbitrary periods of time in both adherent and flowing cell populations. Growth regulation of mammalian cells has been described as “One of the last big unsolved problems in cell biology”⁶⁸. The ability to measure accurately the growth rate of single cells has been the main obstacle in answering this question^{69–71}. Determining the growth patterns of single cells offers answers to some of the most

elusive questions in contemporary cell biology: how cell growth is regulated and how cell size distributions are maintained. The age-old debate is whether the growth rate is constant throughout the life-cycle of a cell (linear growth) or grows proportionally with the cell mass (exponential growth)⁷⁰. Each growth pattern carries its own biological significance: if the growth is linear, cells do not need machinery to maintain homeostasis; however, exponential growth requires checkpoints and regulatory systems to maintain a constant size distribution⁷². The reason that this debate has persisted despite decades of effort is primarily due to the lack of quantitative methods to measure cell mass with the required sensitivity⁷³. A unified, easy-to-use methodology to measure the growth rate of individual adherent cells of various sizes has been lacking. The unique ability of QPI to weigh cells by simply imaging them stems from the fact that the refractive index is linearly proportional to cell density, irrespective of the constitutive molecular species, as pioneered by Davies and Barer in the 1950s^{74,75}. Since the cell phase map is measured with respect to just culture medium, QPI yields the ‘dry mass’ density map of the cellular structure, that is, the density of the non-aqueous content of the cell, which is mainly proteins and lipids⁷⁶. Using this relationship, the dry mass surface density, σ , of the

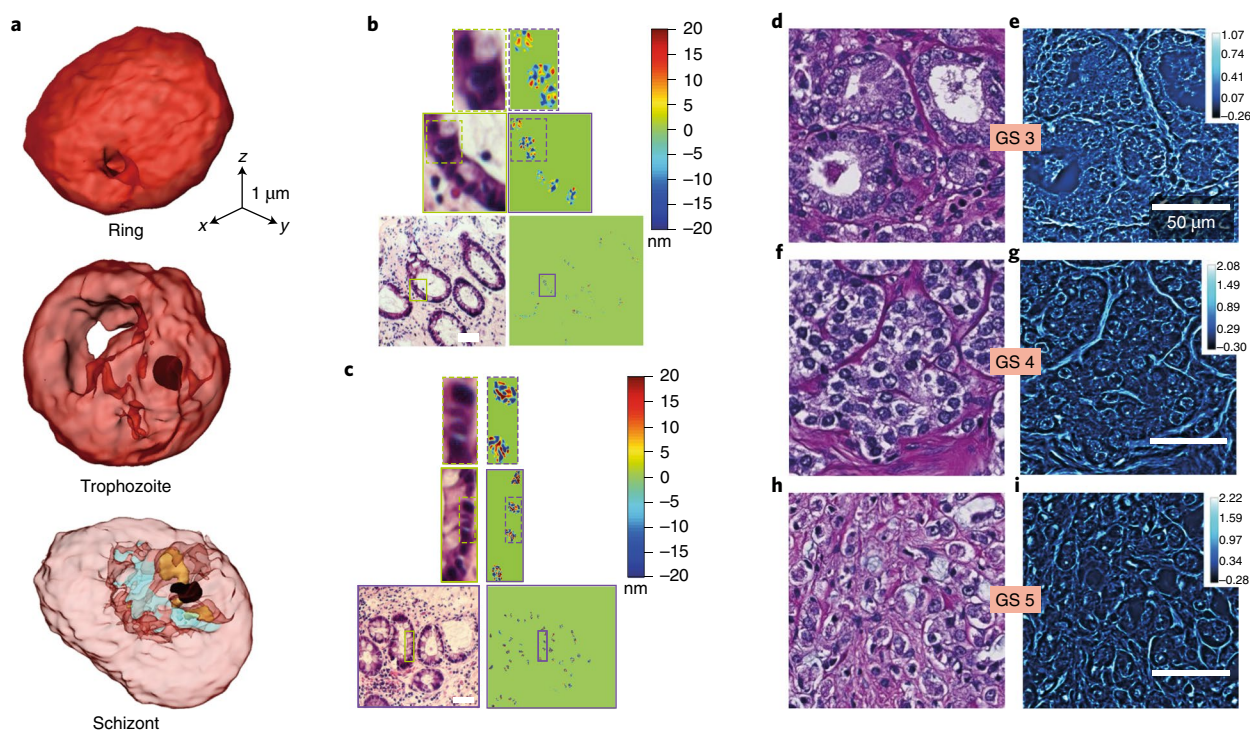


Fig. 5 | Applications of QPI in medicine. **a**, Tomography of RBCs infected with the malaria parasite at various stages of development: ring, trophozoite, schizont, as indicated. **b**, Normal colon epithelial nuclei in an ulcerative colitis patient who did not develop colorectal cancer after seven years (low risk). **c**, Normal colon epithelial nuclei from an ulcerative colitis patient who developed colorectal cancer after seven years (high risk). Scale bars in **b** and **c**, 20 μm . Colour bars indicate optical path length in nm. **d–i**, A side-by-side comparison of hematoxylin and eosin (H&E, left) and spatial light interference microscopy (SLIM, right) images of the same tissue microarray cores show that SLIM images reveal valuable information about the tissue due to the intrinsic contrast. Single strands of stroma stand out in SLIM images as opposed to the uniform pink distribution seen in H&E images. In **d** and **e**, the stroma separating glands appears clearly in SLIM images enabling the classification of the glands as Gleason score 3 (GS 3). Side-by-side comparison of Gleason score 4 (GS 4) tissue microarray cores shown in **f** and **g** also shows the ability of SLIM to detect stroma allowing for better visualization of fusing glands and stromal invasion allowing for accurate Gleason grading. Smaller structures within nuclei, including nucleoli, are more prominent. In the Gleason score 5 (GS 5) images shown in **h** and **i**, the loss of glandularity and presence of epithelial cells in stroma are clearly visible in the SLIM images. Colour bars indicate phase shift in radians. Panel **a** adapted from ref. ¹²⁶, SPIE. Panels **b** and **c** courtesy of Yang Liu, University of Pittsburgh.

cellular matter can be obtained from the measured phase map, ϕ , as $\sigma(x, y) = \frac{\lambda}{2\pi\alpha} \phi(x, y)$, where α is called the refractive increment. In 2011, research from the National Institute of Biomedical Imaging and Bioengineering brought the assumption of a constant α across intracellular species into question and investigated the distribution of α values for “the entire set of known and predicted human proteins.”⁷⁷ The results indicated an extremely narrow distribution: “The distribution is close to Gaussian with a mean of 0.190 ml/g (for unmodified proteins at 589 nm) and a standard deviation of 0.003 ml/g.”⁷⁷ These studies confirmed that it is a very reasonable assumption to use a constant value of $\alpha = 0.19 \text{ ml g}^{-1}$. Thus, σ can be used to quantify cell growth non-invasively, using optical images alone. The accuracy, precision, temporal sensitivity and spatial sensitivity of the σ measurement are governed by the quality of QPI. Figure 4c–e shows the measurements of phase-imaging live cells under osmotic stress, which yields a constant dry mass, despite the water content variation of the cell. Combining QPI with a fluorescent marker that identifies the phases of the cell cycle, cell growth in each phase was measured for the first time⁷⁸.

Label-free tomographic imaging of live cells opens up new directions of investigations, complementary to fluorescence imaging, without limitations due to photobleaching and phototoxicity. Intracellular organelles of eukaryotic cells can also be visualized from 3D refractive index tomograms. For example, the shapes and dry masses of condensed chromosomes of HT-29 and T84 cells in metaphase were measured⁷⁹. Lipid or gold nanoparticles have

distinctly high refractive index contrast values compared with the biomatter, and thus their presence in live cells can be clearly identified from 3D refractive index tomograms. Also, 3D images of SiO_2 microspheres incorporated in cells were measured using the sample rotation method⁵⁵. Recently, the morphology and internal structures of yeast and bacteria have also been measured using 3D QPI techniques^{52,56}. The morphology and structure of chromosomes in the dividing cell was visualized using quantitative orientation-independent differential interference contrast microscopy⁸⁰. Also, QPI was used to distinguish bacteria from sulfur mineral grains⁸¹ and analyse the size of planktons⁸².

Localization and detection of objects smaller than the diffraction-limited size is challenging. Recently, 3D subnanometre localization of absorbing particles was demonstrated using both intensity and phase measurement, for fluorescence super-resolution imaging enhancement⁸³. The sample can even be illuminated with a totally spatially and temporally incoherent illumination scheme leading to a 3D resolution equivalent to fluorescence imaging, at the expense of phase accuracy⁸⁴. Also, rapid holographic detection of viruses and nanoparticles across an ultra-large field of view was demonstrated using a phase contrast mechanism created by self-assembled nanolenses⁸⁵. High sensitivity in measuring phase images has also been exploited to study the wrinkling of a silicone rubber film by motile fibroblasts⁸⁶.

Recently, label-free tomography has been extended to optically thick specimens, such as embryos, brain slices, spheroids

Table 1 | Representative QPI methods and their biomedical applications

Year	Method	Applications
1995	Digitally recorded interference microscopy with automatic phase-shifting (DRIMAPS) ⁷⁶	Cell growth, cell migration ¹⁰⁵
1998	Transport of intensity equation (TIE) ²⁵	Pathology ¹⁰⁶
2004	Fourier phase microscopy (FPM) ¹⁰⁷	Red blood cell dynamics ¹⁰⁸ , cell growth ⁷¹
2005	Hilbert phase microscopy (HPM) ¹⁰⁹	Red blood cell dynamics ¹¹⁰ , tissue refractometry ¹¹¹
2005	Digital holographic microscopy (DHM) ¹¹²	Cell tomography ^{54,57,59} , cancer cell biology ⁸⁷ , neuroscience ⁶⁸ , inflammation ^{94,95} , wound healing ⁹⁹
2006	Diffraction phase microscopy (DPM) ³¹	Cancer prognosis ¹¹³ , malaria ¹¹⁴ , sickle cell anaemia ¹¹⁵
2006	Optical diffraction tomography (ODT) ^{48,50} Tomographic phase microscopy (TPM) ^{51,52,54}	Immunology ⁹⁸ , pharmacology ⁹⁶ , infectious disease ¹⁴ , metabolic disorder — diabetes mellitus ⁹¹ , cell biology ⁵² , neuroscience ⁵²
2009	Quadriwave lateral shearing interferometer (QLSI) ¹¹⁶	Immunology ¹¹⁷
2010	Coherence-controlled holographic microscope (CCHM) ¹¹⁸	Cell biology ¹¹⁹
2011	Spatial light interference microscopy (SLIM) ¹²⁰	Cell biology ⁷⁸ , neuroscience ¹²¹ , cell tomography ³² , cancer diagnosis ¹²²
2011	Wide-field digital interferometry (WFDI)	Genetic diseases — sickle cell disease ⁹⁰
2017	Quantitative phase imaging unit (QPIU)	Microbiology — pathogen ⁹⁹
2017	Gradient light interference microscopy (GLIM) ³³	Developmental biology
2018	Magnified image spatial spectrum microscopy (MISS) ¹²³	Neuroscience

and organoids, which traditionally were imaged fixed with confocal or two-photon fluorescence microscopy. This method, referred to as gradient light interference microscopy (GLIM) was applied to image bovine embryos non-destructively over several days³³ (Fig. 4f). GLIM's principle of operation relies on combining Nomarski microscopy with phase-shifting interferometry to eliminate the incoherent, multiple scattering light, from multiple intensity images. Due to the white-light spectrum, open condenser illumination, GLIM provides sectioning, of the order of 1 μm , in very strongly scattering specimens.

Using off-axis interferometry, recently it has been shown that QPI is a powerful approach for quantifying the efficacy of cell immunotherapy. The time-lapse 3D imaging of a chimeric antigen receptor T cell killing a target cancer cell (leukemic B cell) was obtained using optical diffraction tomography (Fig. 4g). We anticipate that, in time, QPI will be adopted as a routine method in cell biology, in vitro drug testing and automated cell culture monitoring.

Medical applications. The morphologies of live cells are significantly altered by disease states such as viral infection and cancer, and the optical characterization of these alterations using QPI has several advantages over conventional imaging approaches. Because

QPI does not require fixation or sample preparation procedures or exogenous labelling agents, subtle changes in live cells can be monitored for an extended period of time. By measuring cell thickness using QPI, phenotyping of cancer cells was demonstrated⁸⁷. Recently, 3D refractive index tomograms of human alveolar epithelial A549 cells infected with H3N2 influenza viruses have been presented⁸⁸. In addition, 3D refractive index tomograms of healthy and cancerous epithelial cells (CA9-22 and BCC cell lines) were measured and analysed⁸⁹.

Quantitative and label-free imaging capability makes QPI an effective method for blood screening. The optical measurements of 3D refractive index maps of RBCs provide the systematic and correlative analysis of various cellular parameters, such as morphological (cell volume, cell surface area, sphericity index), biochemical (haemoglobin concentration, haemoglobin contents and biomechanical), and cell membrane deformability at the individual cell level. Morphologies of blood cells such as cell shape and cell volume can be quantitatively retrieved. In addition, the measured optical path length information can be translated into haemoglobin concentration. Measuring these RBC parameters using QPI has shown potential for haematology, including sickle cell disease⁹⁰, diabetes⁹¹ and the activation of thrombocytes⁹². Also, it has been shown recently that QPI provides label-free sperm analysis, which can be potentially used in in vitro fertilization⁹³. Furthermore, the quantification of inflammation in dissected tissues and multi-modal imaging of wound healing were demonstrated by analysing the influence of drugs or toxins^{94,95}. More recently, 3D refractive index tomograms of unlabelled cells were used for the study of photodynamic anticancer activity⁹⁶. Figure 5 illustrates QPI diagnosis of malaria-infected RBCs (Fig. 5a), as well as prognosis in the colon (Fig. 5b,c) and prostate (Fig. 5d–i) tissues.

One of the exciting directions of research is combining QPI with artificial intelligence. QPI measures optical path length images and 3D refractive index distributions of cell and tissues, and this information has been used for diagnosis of diseases. Artificial intelligence provides very useful approaches for the analysis of the QPI information, especially due to the quantitative nature of the data, which allows corroborating measurements across instruments, laboratories and geographic sites. Conventional approaches using labelled cells and tissues yield qualitative information, which has low reproducibility and may affect the specimens. For example, inconsistency in biopsy preparation, which results in colour variability, has been recently brought into attention as a limiting factor in achieving fully automated diagnosis⁹⁷.

Recently, 3D refractive index tomograms of white blood cells were analysed with a machine-learning algorithm and showed the classification of white blood cell subtypes including B cells and T cells⁹⁸. Recently, algorithms based on unsupervised deep learning have been employed to analyse images obtained with QPI techniques, including holographic images of the cells surface labelled with molecular-specific microbeads⁹⁹, label-free classification of single-cell kinetic states¹⁰⁰, and diagnosis of soil-transmitted helminths and *Schistosoma haematobium*¹⁰¹. More recently, a convolutional neural network has been used to analyse 2D QPI images of bacteria and identify anthrax spores within a few seconds⁹⁹.

Summary and outlook

QPI offers exciting possibilities for numerous applications in biology and medicine, as discussed in the previous section. Table 1 summarizes in chronological order some of the essential technology developments, along with their biomedical applications. One of the next significant technical goals is super-resolution QPI. Although super-resolution imaging of cells and subcellular organelles have been extensively shown using fluorescence tagging¹⁰², label-free super-resolution imaging remains a challenge. Synthetic aperture approaches in QPI extended the maximum spatial frequency to be

resolved by a factor of two^{52,103}. Yet, it is still limited by the numerical aperture of an objective lens. It is expected that nonlinear interactions, such as pump–probe experiments, may provide an opportunity for breaking the diffraction limit in unlabelled specimens.

The quest for higher phase sensitivity is bound to continue. While shot noise imposes an ultimate limit on the measurement, higher photon fluxes, as well as spatial and temporal averaging, are practical means for achieving orders of magnitude of improvement in the measurement sensitivity. One intriguing question is: can we push the sensitivity of QPI measurements to a level sufficient to detect single molecules?

Another important prospect is the reconstruction of 3D refractive index tomograms in thick, strongly scattering specimens. Opportunities may be presented by developing new methods to reject multiple scattering, or use the multiple light scattering itself for the reconstruction. This achievement could lead to the non-invasive visualization of internal structures in complex samples such as spheroids, organoids, brain slices and model organisms. Exploiting the multiple scattering components one can perhaps achieve subwavelength imaging, by using the conversion of evanescent fields into propagating, far-field information.

The benefit of imaging unlabelled specimens comes at the expense of losing specificity. Aware of this shortcoming, many researchers devoted the extra effort to integrate their QPI instruments with the fluorescence modality. The idea is that the user can employ the fluorescence tag to identify the structures of interest and then continue with the phase imaging channel. This way, the use of the fluorescence, and the photobleaching and phototoxicity that come with it, is reduced, but the specificity is maintained. Recently, QPI has been combined with Raman spectroscopy for studying activation of immune cells¹⁰⁴. Along these lines, a largely unexplored area is using scattering rather than fluorescent markers. If one can tag specifically particular structures in the live cell using nanoparticles of high-enough refractive index contrast, QPI becomes an ideal imaging tool, providing highly specific information, without the limitations associated with fluorescence. For example, such scattering markers can be used indefinitely, with no photobleaching.

In summary, QPI provides essential value to microscopy. The interpretation of the phase signal has proven to deliver important novel parameters for studying physiological processes in living cells, such as transmembrane fluid flux, dry mass and water content changes, intracellular transport as well as tissue structure and density changes. Protein concentrations and growth can be precisely quantified. The morphologies of cells and organelles can be established by phase tomography. Their studies provide invaluable information on the biomechanical characteristics of cell structures and membranes. These data are indicative of biomolecular activity, which can be affected by pathology. We have witnessed extremely promising applications in haematopathology, where the prospect of objective diagnoses that are also robust to specimen preparation, remains highly desirable. It is very likely that, as the technology is transferred from the engineering to the biomedical laboratories, novel, high-impact, currently unexplored applications will surface. Commercialization efforts and application-driven academic collaborations across disciplines are key for these future developments.

Received: 25 February 2018; Accepted: 13 August 2018;
Published online: 27 September 2018

References

- Evanko, D., Heinrichs, A. & Rosenthal, C. Milestones in light microscopy. *Nat. Cell Biol.* **S5–S20** (2009).
- Popescu, G. *Quantitative Phase Imaging of Cells and Tissues* (McGraw-Hill, New York, 2011).
- Abbe, E. *Beiträge zur Theorie des Mikroskops und der mikroskopischen Wahrnehmung*. *Arch. Mikrosk. Anat.* **9**, 413–418 (1873).
- Hell, S. W. & Wichmann, J. Breaking the diffraction resolution limit by stimulated emission: stimulated-emission-depletion fluorescence microscopy. *Opt. Lett.* **19**, 780–782 (1994).
- Tuchin, V. V. & Society of Photo-optical Instrumentation Engineers. *Tissue Optics: Light Scattering Methods and Instruments For Medical Diagnosis* 2nd edn (SPIE/International Society for Optical Engineering, Bellingham, 2007).
- Diaspro, A. *Optical Fluorescence Microscopy* (Springer, Berlin, 2011).
- Kumar, V., Abbas, A. K., Fausto, N. & Aster, J. C. *Robbins and Cotran Pathologic Basis of Disease* (Elsevier Health Sciences, Oxford, 2014).
- Zernike, F. How I discovered phase contrast. *Science* **121**, 345–349 (1955).
- Born, M. & Wolf, E. *Principles of Optics: Electromagnetic Theory of Propagation, Interference and Diffraction of Light* 7th edn (Cambridge Univ. Press, 1999).
- Gabor, D. A new microscopic principle. *Nature* **161**, 777–778 (1948).
- Lohmann, A. *Optische Einseitenübertragung angewandt auf das Gabor-Mikroskop*. *Opt. Acta* **3**, 97–99 (1956).
- Leith, E. N. & Upatnieks, J. Reconstructed wavefronts and communication theory. *J. Opt. Soc. Am.* **52**, 1123–1130 (1962).
- Poon, T.-C. *Digital Holography and Three-dimensional Display: Principles and Applications* (Springer Science & Business Media, New York, 2006).
- Boas, D. A., Pitris, C. & Ramanujam, N. (eds) *Handbook of Biomedical Optics* (CRC Press, Boca Raton, 2016).
- Cuche, E., Bevilacqua, F. & Depeursing, C. Digital holography for quantitative phase-contrast imaging. *Opt. Lett.* **24**, 291–293 (1999).
- Creath, K. Phase-measurement interferometry techniques. *Prog. Opt.* **26**, 349–393 (1988).
- Huang, D. et al. Optical coherence tomography. *Science* **254**, 1178–1181 (1991).
- deBoer, J. F., Milner, T. E., vanGemert, M. J. C. & Nelson, J. S. Two-dimensional birefringence imaging in biological tissue by polarization-sensitive optical coherence tomography. *Opt. Lett.* **22**, 934–936 (1997).
- Izatt, J. A., Kulkarni, M. D., Yazdanfar, S., Barton, J. K. & Welch, A. J. In vivo bidirectional color Doppler flow imaging of picoliter blood volumes using optical coherence tomography. *Opt. Lett.* **22**, 1439–1441 (1997).
- Hitzengerber, C. K. & Fercher, A. F. Differential phase contrast in optical coherence tomography. *Opt. Lett.* **24**, 622–624 (1999).
- Yang, C. H. et al. Interferometric phase-dispersion microscopy. *Opt. Lett.* **25**, 1526–1528 (2000).
- Yang, C. et al. Phase-referenced interferometer with subwavelength and subhertz sensitivity applied to the study of cell membrane dynamics. *Opt. Lett.* **26**, 1271–1273 (2001).
- Choma, M. A., Ellerbee, A. K., Yang, C. H., Creazzo, T. L. & Izatt, J. A. Spectral-domain phase microscopy. *Opt. Lett.* **30**, 1162–1164 (2005).
- Joo, C., Akkin, T., Cense, B., Park, B. H. & de Boer, J. E. Spectral-domain optical coherence phase microscopy for quantitative phase-contrast imaging. *Opt. Lett.* **30**, 2131–2133 (2005).
- Paganin, D. & Nugent, K. A. Noninterferometric phase imaging with partially coherent light. *Phys. Rev. Lett.* **80**, 2586–2589 (1998).
- Takeda, M., Ina, H. & Kobayashi, S. Fourier-transform method of fringe-pattern analysis for computer-based topography and interferometry. *J. Opt. Soc. Am.* **72**, 156–160 (1982).
- Liebling, M., Blu, T. & Unser, M. Complex-wave retrieval from a single off-axis hologram. *J. Opt. Soc. Am. A* **21**, 367–377 (2004).
- Michelson, A. A. & Morley, E. W. On the relative motion of the luminiferous ether. *Am. J. Sci.* **34**, 333–345 (1887).
- Hosseini, P. et al. Pushing phase and amplitude sensitivity limits in interferometric microscopy. *Opt. Lett.* **41**, 1656–1659 (2016).
- A triumph of sensitivity. *Nat. Photon.* **11**, 677 (2017).
- Popescu, G., Ikeda, T., Dasari, R. R. & Feld, M. S. Diffraction phase microscopy for quantifying cell structure and dynamics. *Opt. Lett.* **31**, 775–777 (2006).
- Kim, T. et al. White-light diffraction tomography of unlabelled live cells. *Nat. Photon.* **8**, 256–263 (2014).
- Nguyen, T. H., Kandel, M. E., Rubessa, M., Wheeler, M. B. & Popescu, G. Gradient light interference microscopy for 3D imaging of unlabelled specimens. *Nat. Commun.* **8**, 210 (2017).
- Stockton, P. A., Field, J. J. & Bartels, R. A. Single pixel quantitative phase imaging with spatial frequency projections. *Methods* **136**, 24–34 (2018).
- Yin, Z. Z., Kanade, T. & Chen, M. Understanding the phase contrast optics to restore artifact-free microscopy images for segmentation. *Med. Image Anal.* **16**, 1047–1062 (2012).
- Dubois, F., Requena, M.-L. N., Minetti, C., Monnom, O. & Istasse, E. Partial spatial coherence effects in digital holographic microscopy with a laser source. *Appl. Opt.* **43**, 1131–1139 (2004).
- Mico, V., Zalevsky, Z. & García, J. Common-path phase-shifting digital holographic microscopy: a way to quantitative phase imaging and superresolution. *Opt. Commun.* **281**, 4273–4281 (2008).

38. Greenbaum, A. et al. Imaging without lenses: achievements and remaining challenges of wide-field on-chip microscopy. *Nat. Methods* **9**, 889–895 (2012).
39. Rubin, M., Dardikman, G., Mirsky, S. K., Turko, N. A. & Shaked, N. T. Six-pack off-axis holography. *Opt. Lett.* **42**, 4611–4614 (2017).
40. Chen, S., Li, C. & Zhu, Y. Sensitivity evaluation of quantitative phase imaging: a study of wavelength shifting interferometry. *Opt. Lett.* **42**, 1088–1091 (2017).
41. Sinha, A., Lee, J., Li, S. & Barbastathis, G. Lensless computational imaging through deep learning. *Optica* **4**, 1117–1125 (2017).
42. Rivenson, Y., Zhang, Y., Günaydin, H., Teng, D. & Ozcan, A. Phase recovery and holographic image reconstruction using deep learning in neural networks. *Light Sci. Appl.* **7**, 17141 (2018).
43. Wu, Y. et al. Extended depth-of-field in holographic image reconstruction using deep learning based auto-focusing and phase-recovery. *Optica* **5**, 704–710 (2018).
44. Bohren, C. F. & Huffman, D. R. *Absorption and Scattering of Light by Small Particles* (Wiley, New York, 1983).
45. Ding, H. F., Wang, Z., Nguyen, F., Boppert, S. A. & Popescu, G. Fourier transform light scattering in inhomogeneous and dynamic structures. *Phys. Rev. Lett.* **101**, 238102 (2008).
46. Berne, B. J. & Pecora, R. *Dynamic Light Scattering with Applications to Chemistry, Biology and Physics* (Wiley, New York, 1976).
47. Wang, R. et al. Dispersion-relation phase spectroscopy of intracellular transport. *Opt. Express* **19**, 20571–20579 (2011).
48. Wolf, E. Three-dimensional structure determination of semi-transparent objects from holographic data. *Opt. Commun.* **1**, 153–156 (1969).
49. Fercher, A., Bartelt, H., Becker, H. & Wiltschko, E. Image formation by inversion of scattered field data: experiments and computational simulation. *Appl. Opt.* **18**, 2427–2439 (1979).
50. Lauer, V. New approach to optical diffraction tomography yielding a vector equation of diffraction tomography and a novel tomographic microscope. *J. Microsc.* **205**, 165–176 (2002).
51. Choi, W. et al. Tomographic phase microscopy. *Nat. Methods* **4**, 717–719 (2007).
52. Cotte, Y. et al. Marker-free phase nanoscopy. *Nat. Photon.* **7**, 113–117 (2013).
53. Barty, A., Nugent, K. A., Roberts, A. & Paganin, D. Quantitative phase tomography. *Opt. Commun.* **175**, 329–336 (2000).
54. Charrière, F. et al. Cell refractive index tomography by digital holographic microscopy. *Opt. Lett.* **31**, 178–180 (2006).
55. Kuš, A., Dudek, M., Kemper, B., Kujawińska, M. & Vollmer, A. Tomographic phase microscopy of living three-dimensional cell cultures. *J. Biomed. Opt.* **19**, 046009 (2014).
56. Habaza, M., Gilboa, B., Roichman, Y. & Shaked, N. T. Tomographic phase microscopy with 180 degrees rotation of live cells in suspension by holographic optical tweezers. *Opt. Lett.* **40**, 1881–1884 (2015).
57. Merola, F. et al. Tomographic flow cytometry by digital holography. *Light Sci. Appl.* **6**, e16241 (2017).
58. Horstmeyer, R., Chung, J., Ou, X., Zheng, G. & Yang, C. Diffraction tomography with Fourier ptychography. *Optica* **3**, 827–835 (2016).
59. Kim, M.-K. Tomographic three-dimensional imaging of a biological specimen using wavelength-scanning digital interference holography. *Opt. Express* **7**, 305–310 (2000).
60. Pan, Y., Lankenou, E., Welzel, J., Birngruber, R. & Engelhardt, R. Optical coherence-gated imaging of biological tissues. *IEEE J. Sel. Top. Quantum Electron.* **2**, 1029–1034 (1996).
61. Schmitt, J. M. Optical coherence tomography (OCT): a review. *IEEE J. Sel. Top. Quantum Electron.* **5**, 1205–1215 (1999).
62. Bao, C., Barbastathis, G., Ji, H., Shen, Z. & Zhang, Z. Coherence retrieval using trace regularization. *SIAM J. Imaging Sci.* **11**, 679–706 (2018).
63. Kamilov, U. S. et al. Learning approach to optical tomography. *Optica* **2**, 517–522 (2015).
64. Cotte, Y. et al. Realistic 3D coherent transfer function inverse filtering of complex fields. *Biomed. Opt. Express* **2**, 2216–2230 (2011).
65. Jourdain, P. et al. Determination of transmembrane water fluxes in neurons elicited by glutamate ionotropic receptors and by the cotransporters KCC2 and NKCC1: a digital holographic microscopy study. *J. Neurosci.* **31**, 11846–11854 (2011).
66. Jourdain, P. et al. Simultaneous optical recording in multiple cells by digital holographic microscopy of chloride current associated to activation of the ligand-gated chloride channel GABA_A receptor. *PLoS ONE* **7**, e51041 (2012).
67. Marquet, P., Depaepe, C. & Magistretti, P. J. Review of quantitative phase-digital holographic microscopy: promising novel imaging technique to resolve neuronal network activity and identify cellular biomarkers of psychiatric disorders. *Neurophotonics* **1**, 020901 (2014).
68. Weitzman, J. B. Growing without a size checkpoint. *J. Biol.* **2**, 3 (2003).
69. Godin, M. et al. Using buoyant mass to measure the growth of single cells. *Nat. Methods* **7**, 387–390 (2010).
70. Mitchison, J. M. Single cell studies of the cell cycle and some models. *Theor. Biol. Med. Model.* **2**, 4 (2005).
71. Popescu, G. et al. Optical imaging of cell mass and growth dynamics. *Am. J. Physiol. Cell Physiol.* **295**, C538–C544 (2008).
72. Mitchison, J. M. Growth during the cell cycle. *Int. Rev. Cytol.* **226**, 165–258 (2003).
73. Tzur, A., Kafri, R., LeBleu, V. S., Lahav, G. & Kirschner, M. W. Cell growth and size homeostasis in proliferating animal cells. *Science* **325**, 167–171 (2009).
74. Davies, H. G. & Wilkins, M. H. F. Interference microscopy and mass determination. *Nature* **161**, 541 (1952).
75. Barer, R. Interference microscopy and mass determination. *Nature* **169**, 366–367 (1952).
76. Zicha, D. & Dunn, G. A. An image-processing system for cell behavior studies in subconfluent cultures. *J. Microsc.* **179**, 11–21 (1995).
77. Zhao, H., Brown, P. H. & Schuck, P. On the distribution of protein refractive index increments. *Biophys. J.* **100**, 2309–2317 (2011).
78. Mir, M. et al. Optical measurement of cycle-dependent cell growth. *Proc. Natl Acad. Sci. USA* **108**, 13124–13129 (2011).
79. Sung, Y., Choi, W., Lue, N., Dasari, R. R. & Yaqoob, Z. Stain-free quantification of chromosomes in live cells using regularized tomographic phase microscopy. *PLoS ONE* **7**, e49502 (2012).
80. Shribak, M., Larkin, K. G. & Biggs, D. Mapping optical path length and image enhancement using quantitative orientation-independent differential interference contrast microscopy. *J. Biomed. Opt.* **22**, 016006 (2017).
81. Bedrossian, M., Lindensmith, C. & Nadeau, J. L. Digital holographic microscopy, a method for detection of microorganisms in plume samples from Enceladus and other icy worlds. *Astrobiology* **17**, 913–925 (2017).
82. Yourassowsky, C. & Dubois, F. High throughput holographic imaging-in-flow for the analysis of a wide plankton size range. *Opt. Express* **22**, 6661–6673 (2014).
83. Bon, P. et al. Three-dimensional nanometre localization of nanoparticles to enhance super-resolution microscopy. *Nat. Commun.* **6**, 7764 (2015).
84. Bon, P., Aknoun, S., Monneret, S. & Wattellier, B. Enhanced 3D spatial resolution in quantitative phase microscopy using spatially incoherent illumination. *Opt. Express* **22**, 8654–8671 (2014).
85. Mudanyali, O. et al. Wide-field optical detection of nanoparticles using on-chip microscopy and self-assembled nanolenses. *Nat. Photon.* **7**, 247–254 (2013).
86. Yu, X. et al. Measurement of the traction force of biological cells by digital holography. *Biomed. Opt. Express* **3**, 153–159 (2012).
87. Kemper, B. et al. Investigation of living pancreas tumor cells by digital holographic microscopy. *J. Biomed. Opt.* **11**, 034005–034008 (2006).
88. Simon, B., Debailleul, M., Beghin, A., Tourneur, Y. & Haerberle, O. High-resolution tomographic diffractive microscopy of biological samples. *J. Biophoton.* **3**, 462–467 (2010).
89. Hsu, W.-C., Su, J.-W., Chang, C.-C. & Sung, K.-B. Investigating the backscattering characteristics of individual normal and cancerous cells based on experimentally determined three-dimensional refractive index distributions. *Proc. SPIE* **8553**, 85531O (2012).
90. Shaked, N. T., Satterwhite, L. L., Truskey, G. A., Wax, A. P. & Telen, M. J. Quantitative microscopy and analysis of sickle red blood cells performed by wide field digital interferometry. *J. Biomed. Opt.* **16**, 030506 (2011).
91. Lee, S. et al. Refractive index tomograms and dynamic membrane fluctuations of red blood cells from patients with diabetes mellitus. *Sci. Rep.* **7**, 1039 (2017).
92. Khan, S., Jesacher, A., Nussbaumer, W., Bernet, S. & Ritsch-Marte, M. Quantitative analysis of shape and volume changes in activated thrombocytes in real time by single-shot spatial light modulator-based differential interference contrast imaging. *J. Biophoton.* **4**, 600–609 (2011).
93. Haifler, M. et al. Interferometric phase microscopy for label-free morphological evaluation of sperm cells. *Fertil. Steril.* **104**, 43–47.e42 (2015).
94. Lenz, P. et al. Digital holographic microscopy quantifies the degree of inflammation in experimental colitis. *Integr. Biol.* **5**, 624–630 (2013).
95. Bettenworth, D. et al. Quantitative stain-free and continuous multimodal monitoring of wound healing in vitro with digital holographic microscopy. *PLoS ONE* **9**, e107317 (2014).
96. Kwon, S. et al. Mitochondria-targeting indolizino [3,2-c] quinolines as novel class of photosensitizers for photodynamic anticancer activity. *Eur. J. Med. Chem.* **148**, 116–127 (2018).
97. Madabhushi, A. & Lee, G. Image analysis and machine learning in digital pathology: challenges and opportunities. *Med. Image Anal.* **33**, 170–175 (2016).
98. Yoon, J. et al. Identification of non-activated lymphocytes using three-dimensional refractive index tomography and machine learning. *Sci. Rep.* **7**, 6654 (2017).

99. Jo, Y. et al. Holographic deep learning for rapid optical screening of anthrax spores. *Sci. Adv.* **3**, e1700606 (2017).
100. Hejna, M., Jorapur, A., Song, J. S. & Judson, R. L. High accuracy label-free classification of single-cell kinetic states from holographic cytometry of human melanoma cells. *Sci. Rep.* **7**, 11943 (2017).
101. Holmström, O. et al. Point-of-care mobile digital microscopy and deep learning for the detection of soil-transmitted helminths and *Schistosoma haematobium*. *Global Health Action* **10**, 1337325 (2017).
102. Huang, B., Bates, M. & Zhuang, X. Super resolution fluorescence microscopy. *Annu. Rev. Biochem.* **78**, 993–1016 (2009).
103. Alexandrov, S., Hillman, T., Gutzler, T. & Sampson, D. Synthetic aperture Fourier holographic optical microscopy. *Phys. Rev. Lett.* **97**, 168102 (2006).
104. Pavillon, N., Hobro, A. J., Akira, S. & Smith, N. I. Noninvasive detection of macrophage activation with single-cell resolution through machine learning. *Proc. Natl Acad. Sci. USA* <https://doi.org/10.1073/pnas.1711872115> (2018).
105. Dunn, G. A. & Zicha, D. Dynamics of fibroblast spreading. *J. Cell Sci.* **108**, 1239–1249 (1995).
106. Greenbaum, A. et al. Wide-field computational imaging of pathology slides using lens-free on-chip microscopy. *Sci. Transl. Med.* **6**, 267ra175 (2014).
107. Popescu, G. et al. Fourier phase microscopy for investigation of biological structures and dynamics. *Opt. Lett.* **29**, 2503–2505 (2004).
108. Popescu, G., Badizadegan, K., Dasari, R. R. & Feld, M. S. Observation of dynamic subdomains in red blood cells. *J. Biomed. Opt. Lett.* **11**, 040503 (2006).
109. Ikeda, T., Popescu, G., Dasari, R. R. & Feld, M. S. Hilbert phase microscopy for investigating fast dynamics in transparent systems. *Opt. Lett.* **30**, 1165–1168 (2005).
110. Popescu, G. et al. Erythrocyte structure and dynamics quantified by Hilbert phase microscopy. *J. Biomed. Opt. Lett.* **10**, 060503 (2005).
111. Lue, N. et al. Tissue refractometry using Hilbert phase microscopy. *Opt. Lett.* **32**, 3522–3524 (2007).
112. Marquet, P. et al. Digital holographic microscopy: a noninvasive contrast imaging technique allowing quantitative visualization of living cells with subwavelength axial accuracy. *Opt. Lett.* **30**, 468–470 (2005).
113. Uttam, S. et al. Early prediction of cancer progression by depth-resolved nanoscale mapping of nuclear architecture from unstained tissue specimens. *Cancer Res.* **75**, 4718–4727 (2015).
114. Park, Y. K. et al. Refractive index maps and membrane dynamics of human red blood cells parasitized by *Plasmodium falciparum*. *Proc. Natl Acad. Sci. USA* **105**, 13730–13735 (2008).
115. Hosseini, P. et al. Cellular normoxic biophysical markers of hydroxyurea treatment in sickle cell disease. *Proc. Natl Acad. Sci. USA* **113**, 9527–9532 (2016).
116. Bon, P., Maucort, G., Wattellier, B. & Monneret, S. Quadriwave lateral shearing interferometry for quantitative phase microscopy of living cells. *Opt. Express* **17**, 13080–13094 (2009).
117. Mitchell, S., Roy, K., Zangle, T. A. & Hoffmann, A. Nongenetic origins of cell-to-cell variability in B lymphocyte proliferation. *Proc. Natl Acad. Sci. USA* **115**, E2888–E2897 (2018).
118. Kolman, P. & Chmelik, R. Coherence-controlled holographic microscope. *Opt. Express* **18**, 21990–22004 (2010).
119. Štrbková, L. et al. The adhesion of normal human dermal fibroblasts to the cyclopropylamine plasma polymers studied by holographic microscopy. *Surf. Coat. Technol.* **295**, 70–77 (2016).
120. Wang, Z. et al. Spatial light interference microscopy (SLIM). *Opt. Express* **19**, 1016–1026 (2011).
121. Mir, M. et al. Label-free characterization of emerging human neuronal networks. *Sci. Rep.* **4**, 04434 (2014).
122. Majeed, H., Nguyen, T. H., Kandel, M. E., Kajdacsy-Balla, A. & Popescu, G. Label-free quantitative evaluation of breast tissue using spatial light interference microscopy (SLIM). *Sci. Rep.* **8**, 6875 (2018).
123. Majeed, H. et al. Magnified image spatial spectrum (MISS) microscopy for nanometer and millisecond scale label-free imaging. *Opt. Express* **26**, 5423–5440 (2018).
124. Kim, K. et al. Optical diffraction tomography techniques for the study of cell pathophysiology. *J. Biomed. Photon. Eng.* **2**, 2 (2016).
125. Kim, K. et al. Three dimensional label-free imaging and quantification of lipid droplets in live hepatocytes. *Sci. Rep.* **6**, 36815 (2016).
126. Kim, K. et al. High-resolution three-dimensional imaging of red blood cells parasitized by *Plasmodium falciparum* and in situ hemozoin crystals using optical diffraction tomography. *J. Biomed. Opt.* **19**, 0111005 (2013).

Acknowledgements

Y.K.P. was supported by the National Research Foundation of Korea (2017M3C1A3013923, 2015R1A3A2066550, 2017K000396). G.P. was supported by the National Science Foundation (STC CBET 0939511, NSF BRAIN EAGER DBI 1450962, IIP-1353368).

Competing interests

Y.K.P. has financial interest in Tomocube. C.D. has financial interest in Lyncee Tech and Nanolive. G.P. has financial interest in Phi Optics. All these companies commercialize QPI instruments.

Additional information

Reprints and permissions information is available at www.nature.com/reprints.

Correspondence should be addressed to G.P.

Publisher's note: Springer Nature remains neutral with regard to jurisdictional claims in published maps and institutional affiliations.

© Springer Nature Limited 2018